**Electronic Supplementary Material (ESI) for Energy & Environmental Science.
This journal is © The Royal Society of Chemistry 2024**

Electronic Supplementary Information

Unraveling interfacial compatibility of ultrahigh nickel cathode and chloride solid electrolyte for stable all-solid-state lithium battery

Feng Li[1], Ye-Chao Wu[2, 3], Xiao-Bin Cheng[2], Yihong Tan[4], Jin-Da Luo[2], Ruijun Pan[3], Tao Ma[5], Lei-Lei Lu[1], Xiaolei Wen[6], Zheng Liang[4] *, Hong-Bin Yao[1, 2] *

[1]*Division of Nanomaterials and Chemistry, Hefei National Research Center for Physical Sciences at the Microscale, University of Science and Technology of China, Hefei, Anhui 230026, China*

[2]*Department of Applied Chemistry, University of Science and Technology of China, Hefei, Anhui 230026, China*

[3]*Hefei Gotion High-tech Power Energy Co., Ltd. Hefei, Anhui 230012, China*

[4]*Frontiers Science Center for Transformative Molecules, School of Chemistry and Chemical Engineering, Shanghai Jiao Tong University, Shanghai 200240, China*

[5]*Engineering Research Center of High-frequency Soft Magnetic Materials and Ceramic Powder Materials of Anhui Province, School of Chemistry and Material Engineering, Chaohu University, Hefei, 238024, China*

[6]*Center for Micro and Nanoscale Research and Fabrication, University of Science and Technology of China, Hefei, Anhui 230026, China*

F.L., Y.-C.W., X.C., and Y.T. contributed equally to this work.

* Corresponding authors' email: yhb@ustc.edu.cn, liangzheng06@sjtu.edu.cn

Experimental Section

Synthesis of Li_2TaCl_7 SEs. The Li_2TaCl_7 were obtained by ball milling LiCl (anhydrous, Aladdin) and $TaCl_5$ (anhydrous, Aladdin). The ratio of LiCl and $TaCl_5$ powders was set as 2:1 and mixed and then loaded into tungsten carbide pots and ball-milled at 450 rpm for 180 h. The mass ratio of tungsten carbide ball mill beads to the precursors is 55:1. The obtained fine solid electrolyte powders were collected and stored in the glovebox for further application and characterization. All of the preparation processes were conducted in an argon-filled glove box with H_2O and O_2 concentrations less than 0.1 ppm.

Characterizations. The obtained solid electrolyte powders were cold-pressed into 10 mm diameter pellets by a hydraulic press (YLJ-15T-LD, Hefei Kejing Materials Technology Co., Ltd.) at 370 MPa for 3 minutes for alternating current (AC) impedance measurement. The ionic conductivity and activation energy were obtained by impedance in the temperature range from 25 to 60 °C with an applied frequency of 1 Hz to 7 MHz and a constant voltage of 20 mV using a Bio-Logic VMP3. Powder X-ray diffraction patterns were obtained by the Philips X'Pert PRO SUPER X-ray diffractometer using Cu Kα radiation (λ =1.54178 Å). The exposed morphologies of ASSLB composite cathodes with different cycled states in depth were captured with the application of Ga^+ with a 30 kV focused ion beam (FIB, ORION Nanofab, Zeiss). Prior to the measurement, the cathodes were dismantled from the ASSLBs and stuck on the sample tables carefully in an argon-filled glovebox with H_2O and O_2 concentrations less than 0.1 ppm.

Electrochemical measurements of ASSLBs. Single-crystal $LiNi_{0.92}Co_{0.05}Mn_{0.03}O_2$ (S-NCM92, provided by Hefei Gotion High-tech Power Energy Co., Ltd.) was firstly mixed with Li_2TaCl_7 and polytetrafluoroethylene (PTFE) (Guangdong Canrd New Energy Technology Co., Ltd.) with a mass ratio of 75:22:3 and then mixed by a miniature vibration mixer (MSK-SFM-12 M, Hefei Kejing Materials Technology Co., Ltd) for 60 min as cathode composite powders. 100 mg of Li_2TaCl_7 powder was first placed into a polyetheretherketone (PEEK) model (10 mm diameter) and pressed at 1.5 tons for 1 min to form a SE layer. The composite cathode powder with a range of areal capacity of 1-5 mAh cm^{-2} was then spread over the surface of the Li_2TaCl_7 and pressed at 2.5 tons for another 3 min. 40 mg of Li_6PS_5Cl powder was dispersed evenly on the other surface of the Li_2TaCl_7 layer and then pressed at 3 tons for 3 min. Then, a piece of In foil (0.1 mm thickness, 10 mm diameter, 3A Materials) was attached to the surface of Li_6PS_5Cl. A Li foil (6 mm diameter, China Energy Lithium Co., Ltd.) with a weight ratio of Li: In=1:50 was subsequently attached to the In foil. Subsequently, the ASSLB was pressed at 1 ton for

another 1 min and then placed into a custom-made stainless-steel casing (Ningbo Zhengli New Energy Technology Co., Ltd.) with a constantly applied pressure of 100 MPa for 24 hours to form the Li-In alloy. The ASSLB was placed into a custom-made stainless-steel casing for galvanostatic cycling. Galvanostatic cycling (current density: 0.191, 1, and 3 mA cm^{-2}) of the ASSLBs was conducted at 30 °C with a constantly applied pressure of 100 MPa. The voltage range of the cycling was 2.8-4.1 V, 2.8-4.3 V, 2.8-4.6 V, and 2.8-4.8 V versus Li^+/Li using a LAND-CT2001A and Neware-CT-4008T battery cycler. For the aging of ASSLBs, galvanostatic charging was conducted at a current density of 0.191 mA cm^{-2}, followed by constant voltage charging and aging at the designated cut-off voltage for a specified duration. All of the preparation processes were conducted in an argon-filled glove box with H_2O and O_2 concentrations less than 0.1 ppm.

Time-of-flight secondary ion mass spectrometry (ToF-SIMS). For the time-of-flight secondary-ion mass spectrometry (ToF-SIMS) studies, ION-ToF-SIMS 5-100 was used with the pressure of the analysis chamber below 1.1×10^{-9} mbar. The imaging with delay extraction mode with pulsed 30 keV Bi^{3+} (0.48 pA pulsed current) ion beam and a cycle time of 100 μs was applied for analysis. To minimize the effect of mass interference, the spectrometry (bunched) mode was used for surface analysis to enable a high signal intensity and a high mass resolution. The analysis area was set to 100×100 μm^2 and rasterized with 128×128 pixels, and every patch was analyzed with 1 frame and 1 shot per pixel and frame. The primary ion current was ca. 0.48 pA, and the stop condition was set to a primary ion dose of 10^{12} ions cm^2. To quantitatively compare the specific signal intensity, we collected 10 mass spectra at different areas on each cathode.

Supplementary Figures

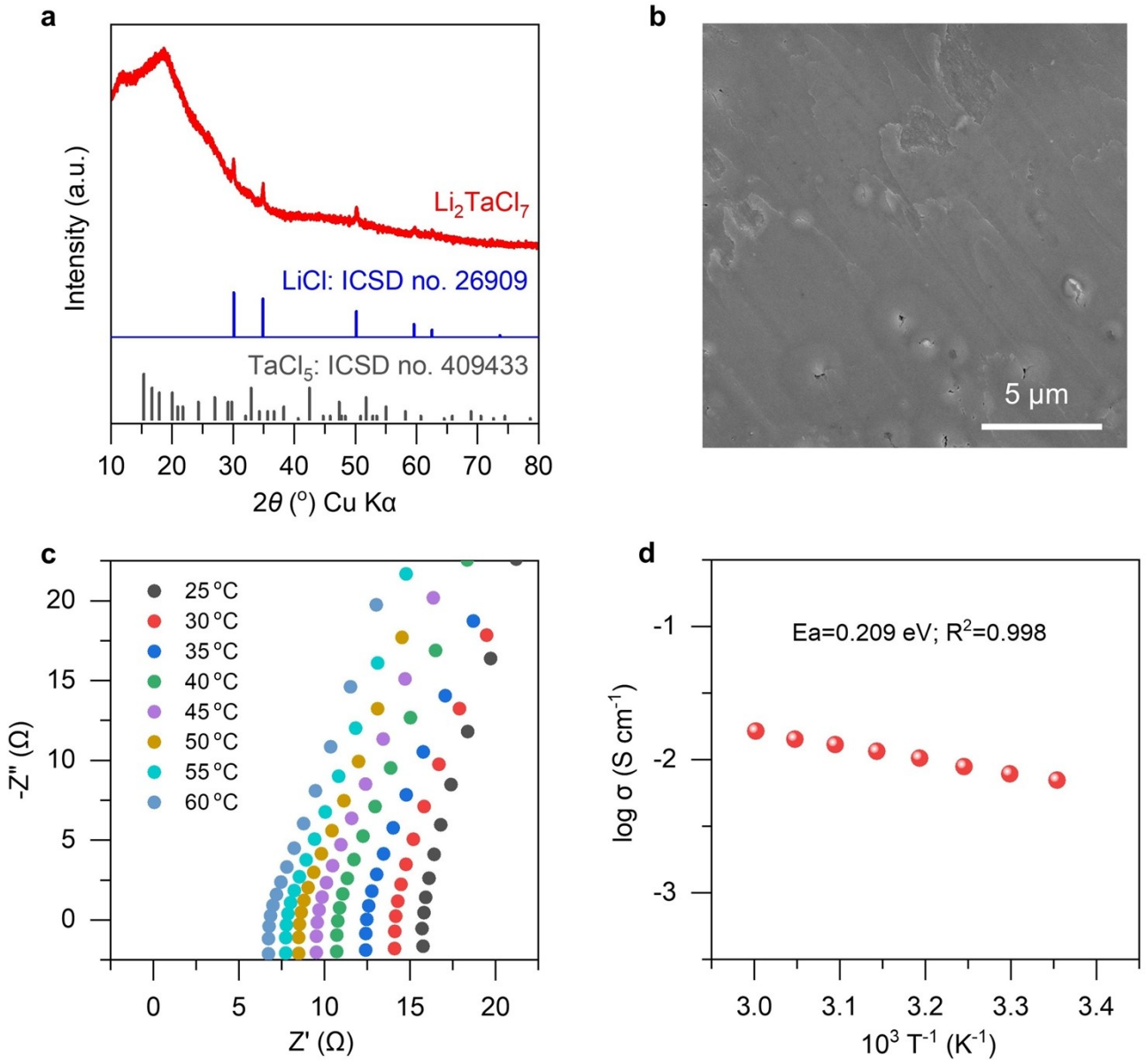

Fig. S1 Characterization of the Li_2TaCl_7. a, PXRD patterns of Li_2TaCl_7. The representative diffraction peaks patterns can be indexed with LiCl (ICSD no. 26909). **b**, SEM images for the surface of cold-pressed Li_2TaCl_7 pellet. **c**, Nyquist plots of the EIS measurement results of Li_2TaCl_7 with nonreversible electrodes in the temperature range from 25 to 60 °C. **d**, Arrhenius plot of ionic conductivities of the Li_2TaCl_7. The ionic conductivity of Li_2TaCl_7 at room temperature is around 7.07 mS/cm.

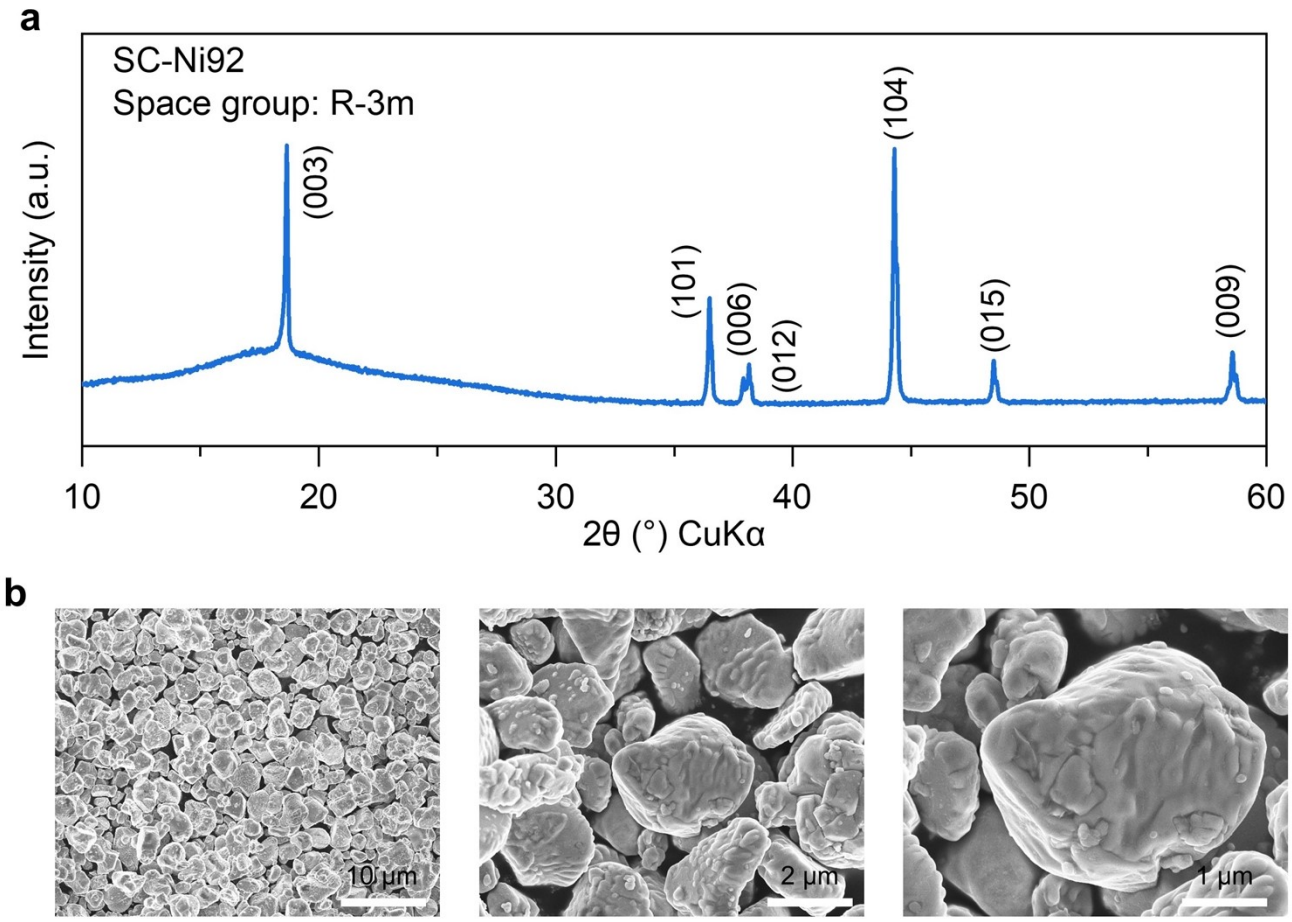

Fig. S2 Characterizations of the S-NMC92. a, PXRD pattern of S-NMC92 powders. **b**, SEM images of S-NMC92 powders.

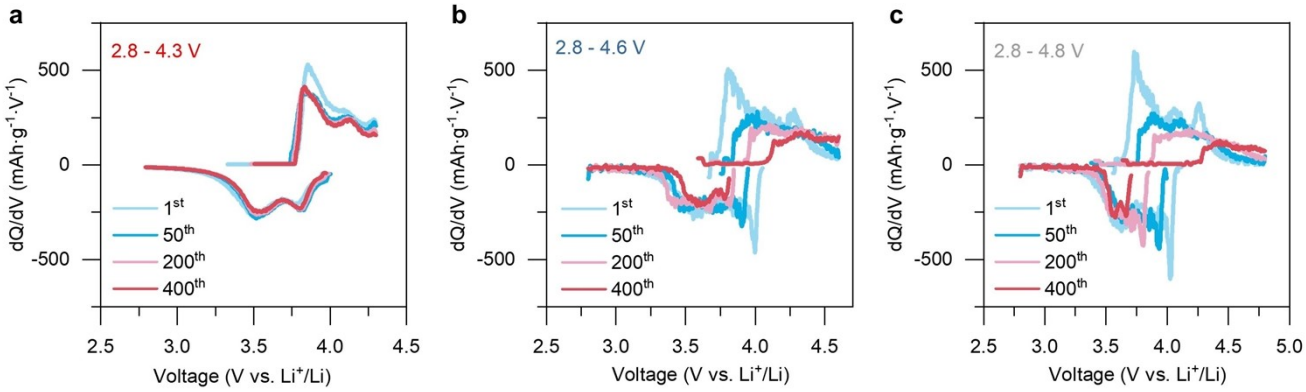

Fig. S3 a-c, Representative corresponding normalized dQ/dV curves of ASSLBs cycled with cut-off charging voltages of 4.3, 4.6, and 4.8 V, respectively.

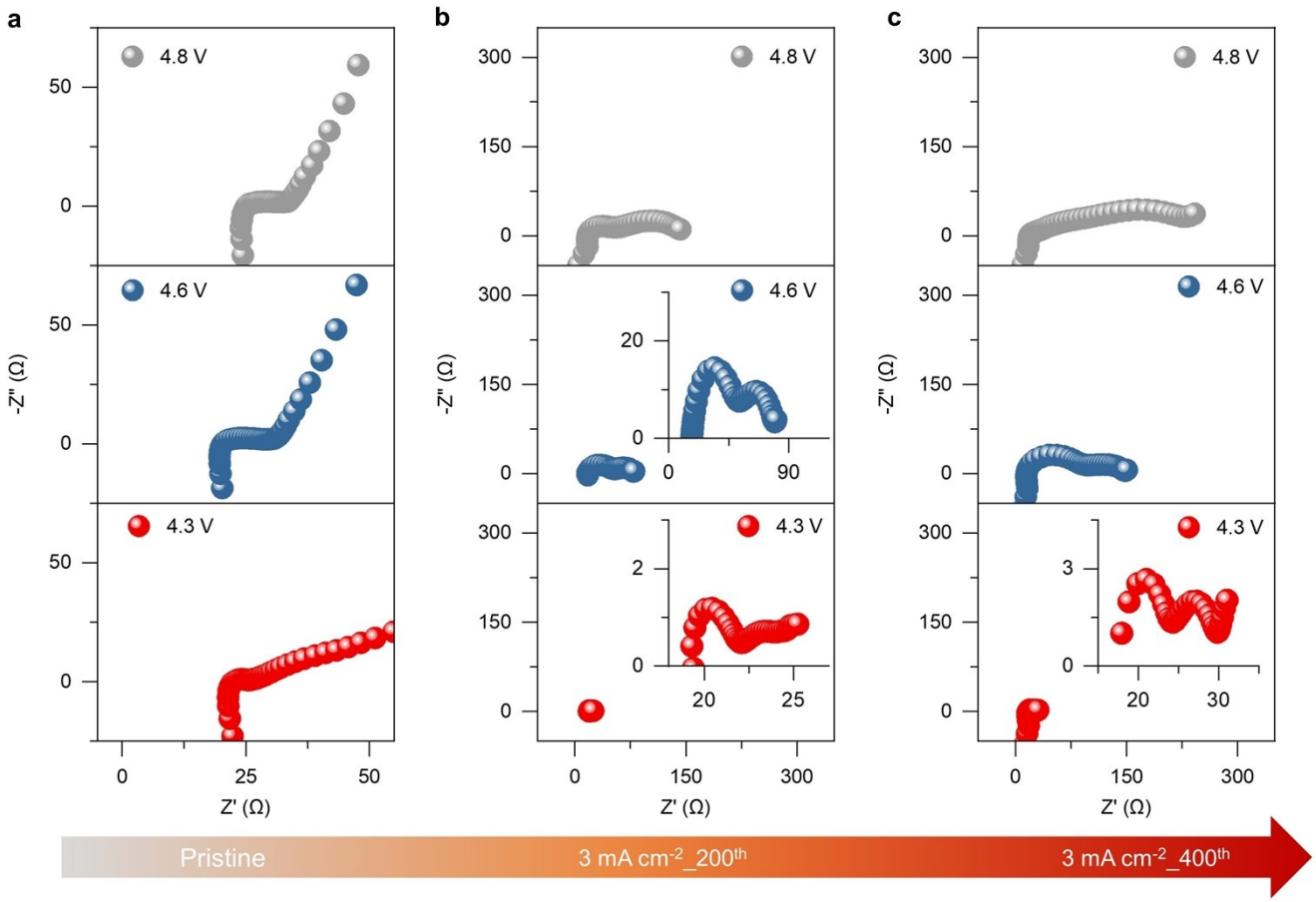

Fig. S4 Evolution of internal resistance of ASSLBs during the cycling process. **a-c**, Nyquist plots of the EIS measurement results of ASSLBs under pristine, 200th, and 400th cycle state.

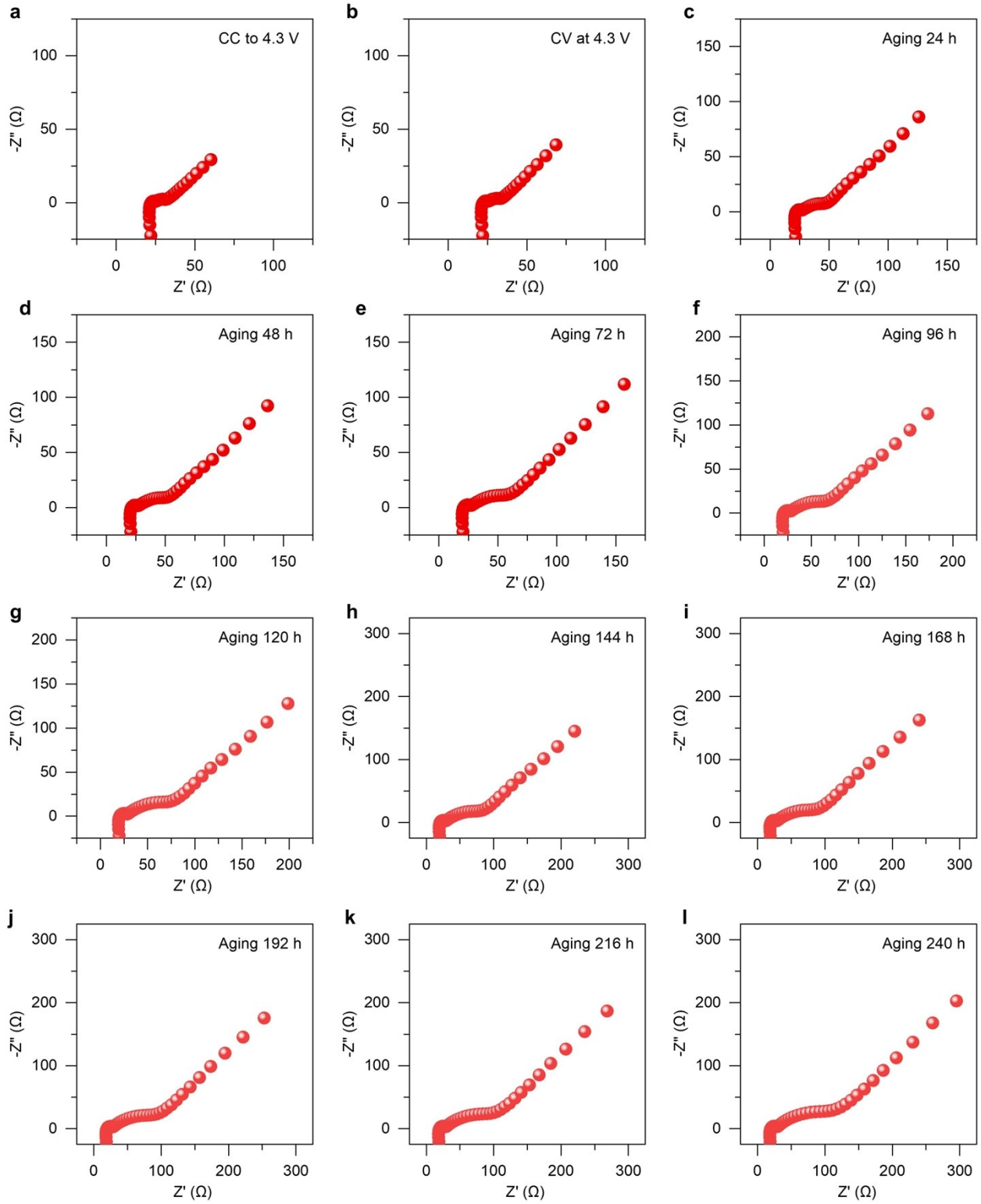

Fig. S5 a-l, Nyquist plots of the EIS measurement results of ASSLBs during the aging process with a constant voltage of 4.3 V.

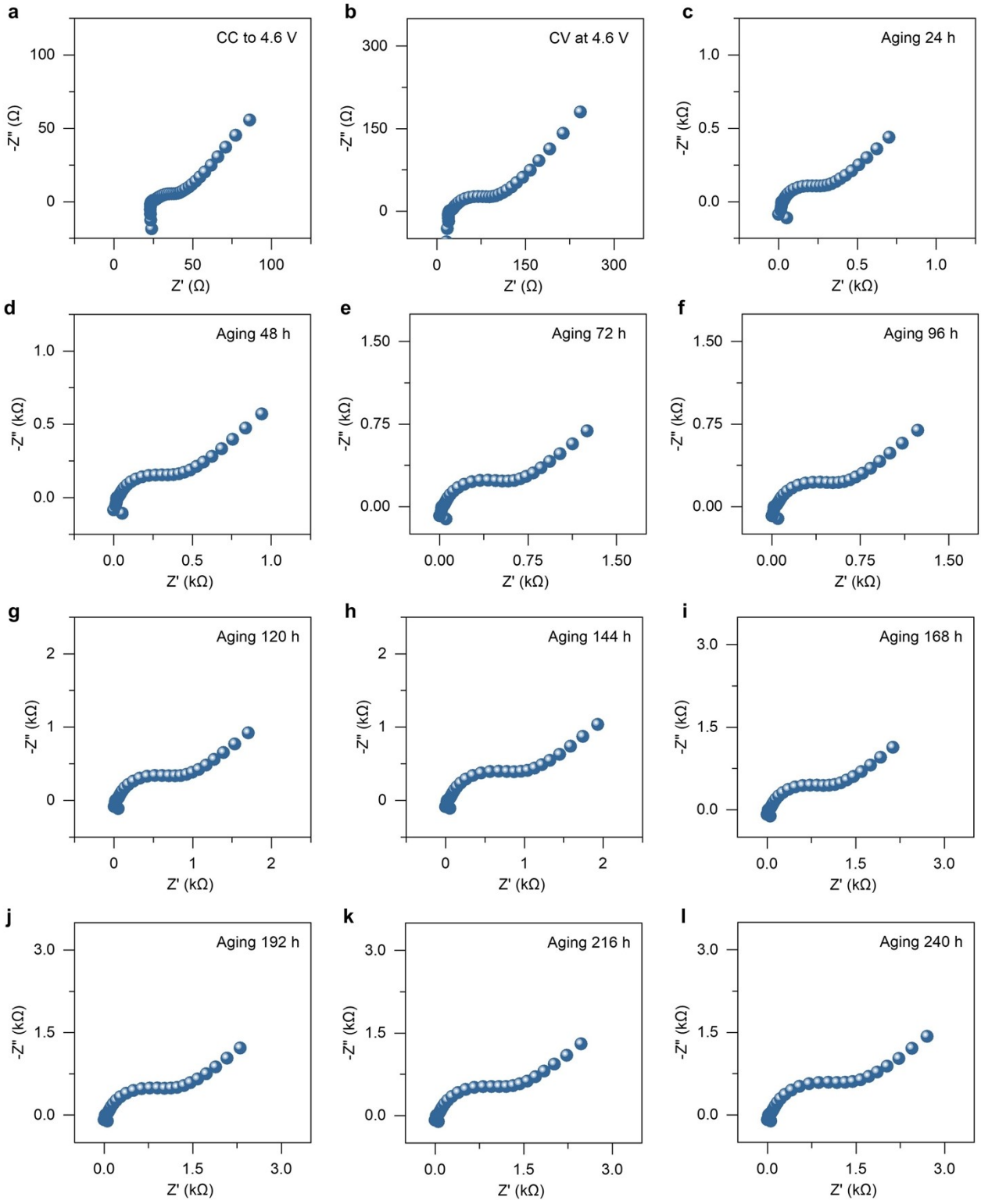

Fig. S6 a-l, Nyquist plots of the EIS measurement results of ASSLBs during the aging process with a constant voltage of 4.6 V.

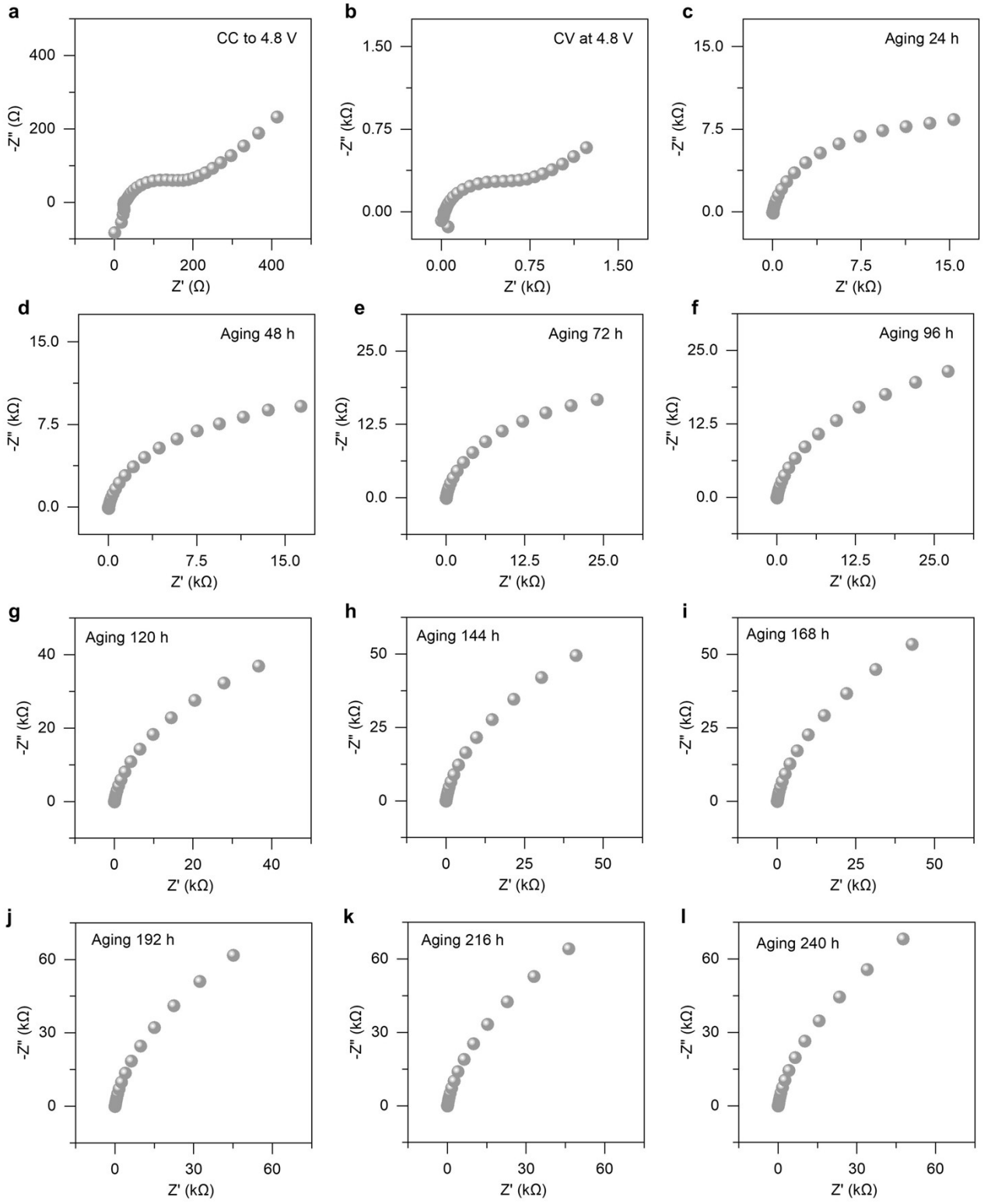

Fig. S7 a-l, Nyquist plots of the EIS measurement results of ASSLBs during the aging process with a constant voltage of 4.8 V.

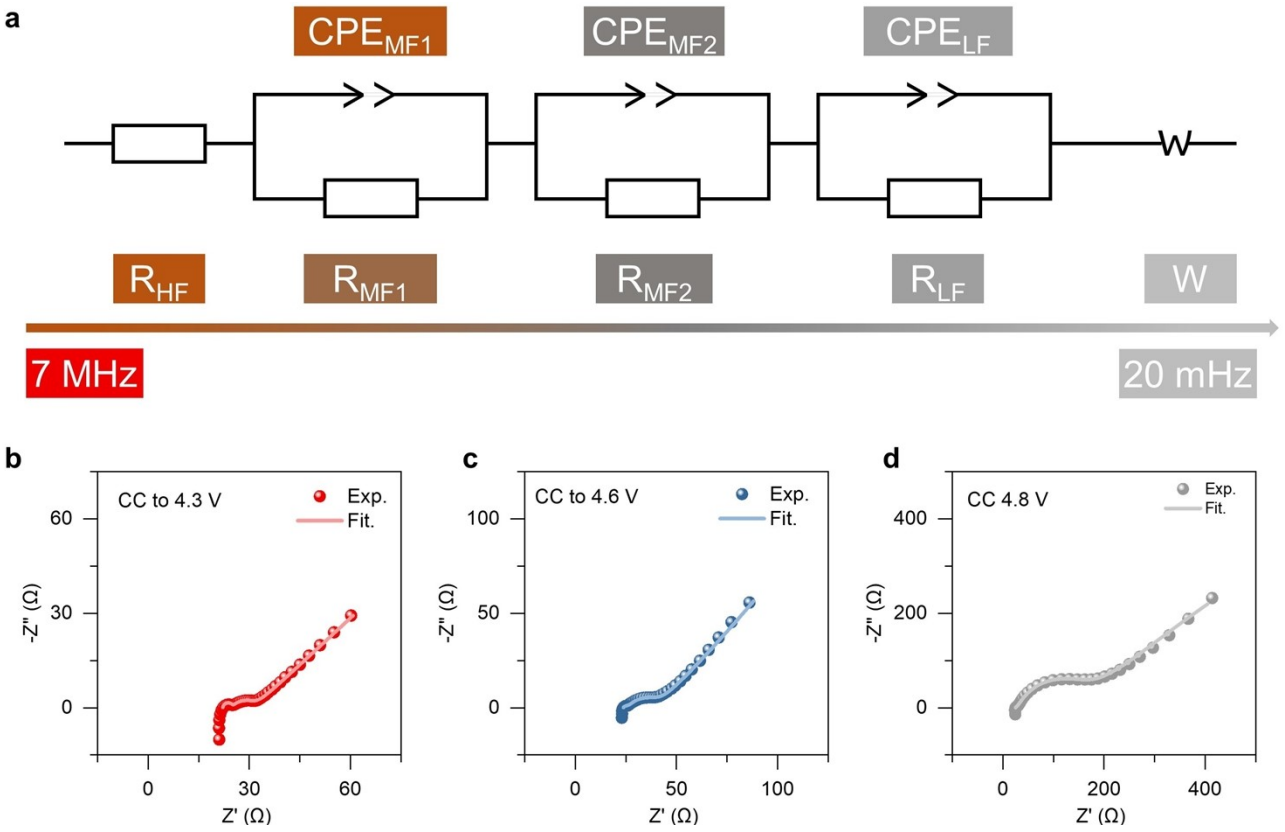

Fig. S8 a, The equivalent circuit employed to fit the Nyquist plots of the EIS results of ASSLBs. **b-d**, Representative fitted results of Nyquist plots of the EIS results of ASSLBs with the cut-off voltage of 4.3, 4.6, and 4.8 V.

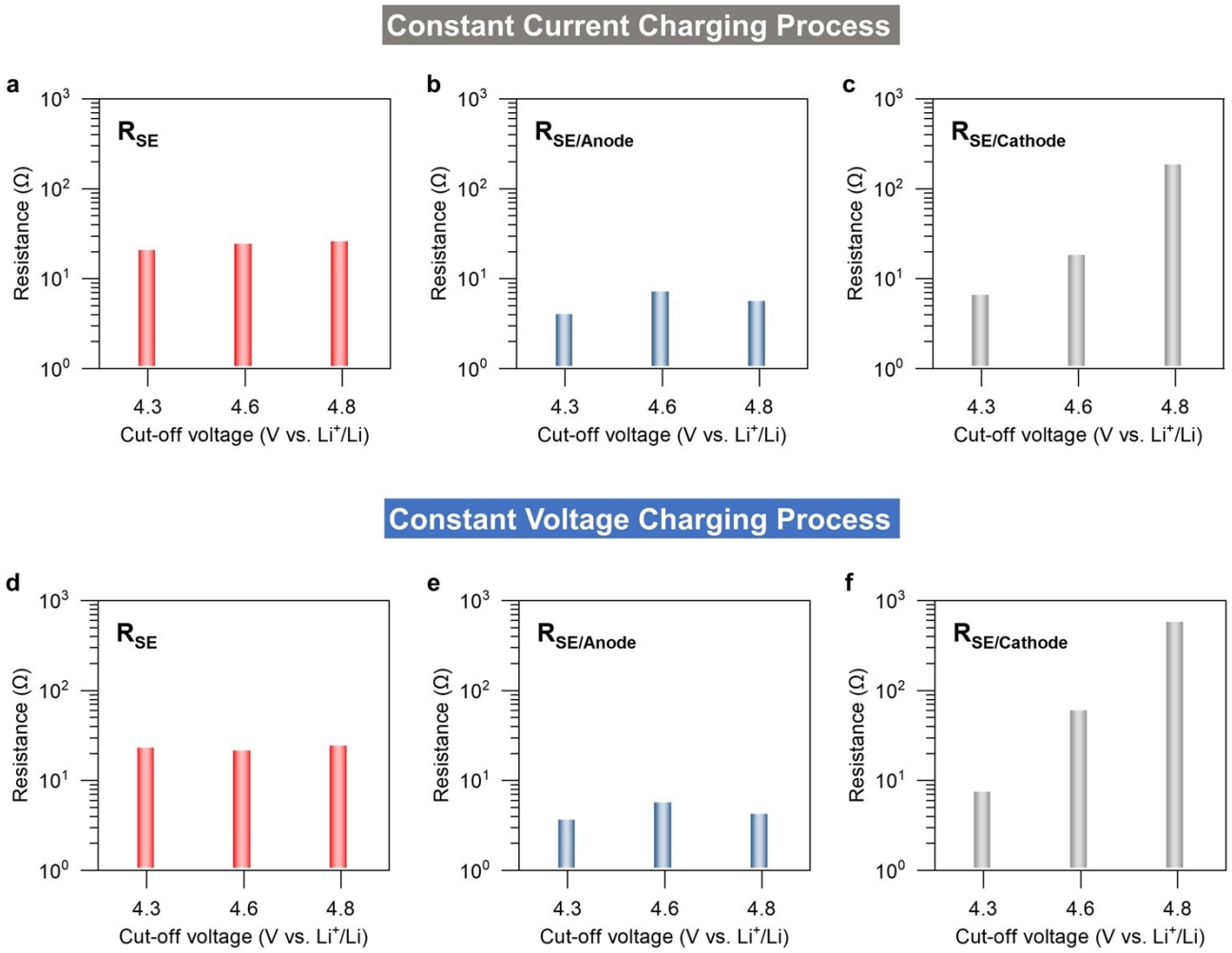

Fig. S9 a-c, The fitted resistance values of ASSLBs with constant current charged to 4.3, 4.6, and 4.8 V. **d-f**, The fitted resistance values of ASSLBs with constant voltage charged to 4.3, 4.6, and 4.8 V.

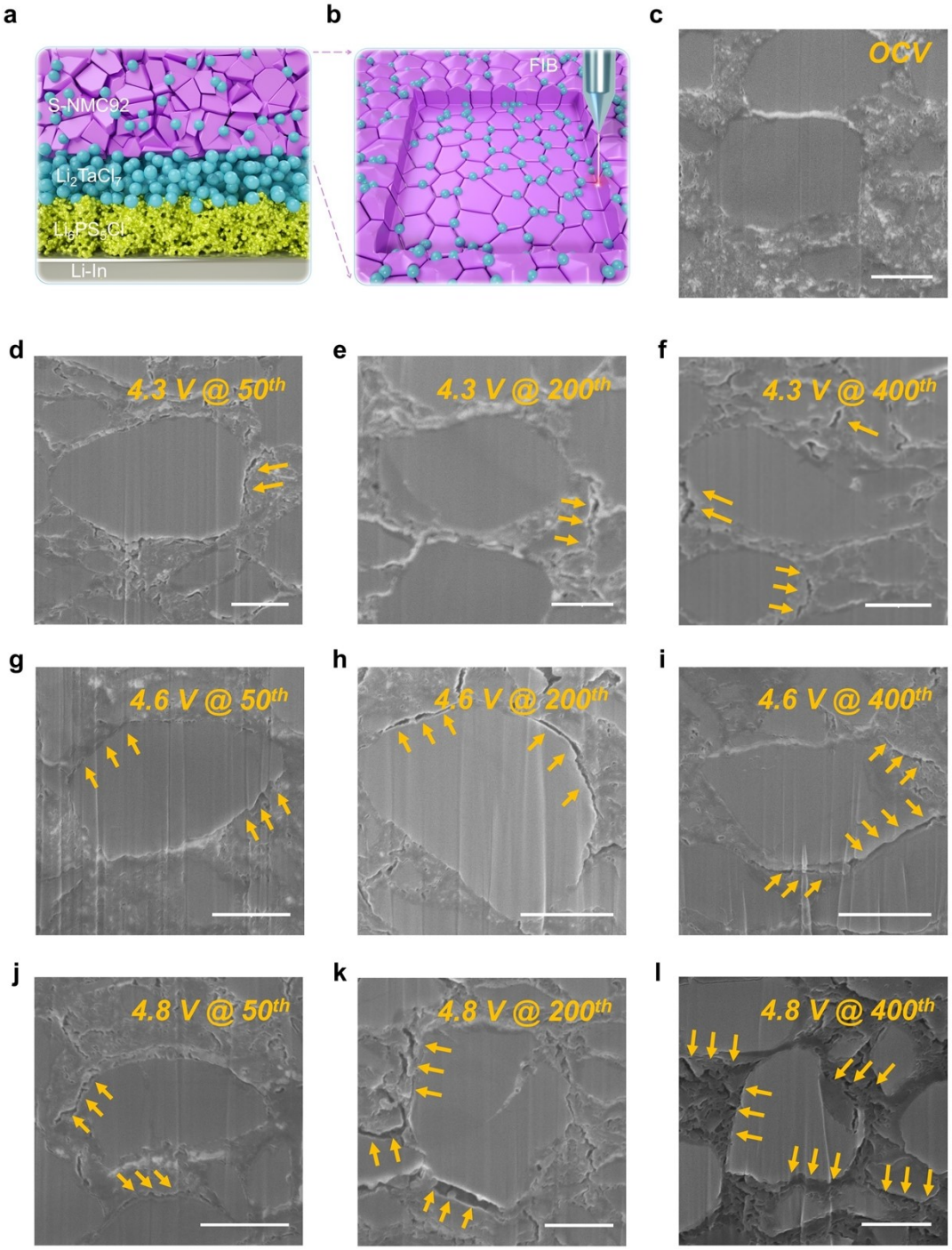

Fig. S10 a-b, Schematic illustration of the fabricated ASSLBs and the Focused ion beam technique used to expose the inside cathode. **c**, SEM image of the exposed surface of the pristine cathode. **d-f**, SEM images of the exposed surface of the cathode cycled with the charging voltage of 4.3 V at the 50th, 200th, and 400th cycle. **g-i**, SEM images of the exposed surface of the cathode cycled with the charging voltage of 4.6 V at the 50th, 200th, and 400th cycle. **j-l**, SEM images of the exposed surface of the cathode cycled with the charging voltage of 4.8 V at the 50th, 200th, and 400th cycle. The physical contact loss was marked by yellow arrows. Scale bar: 1 μm.

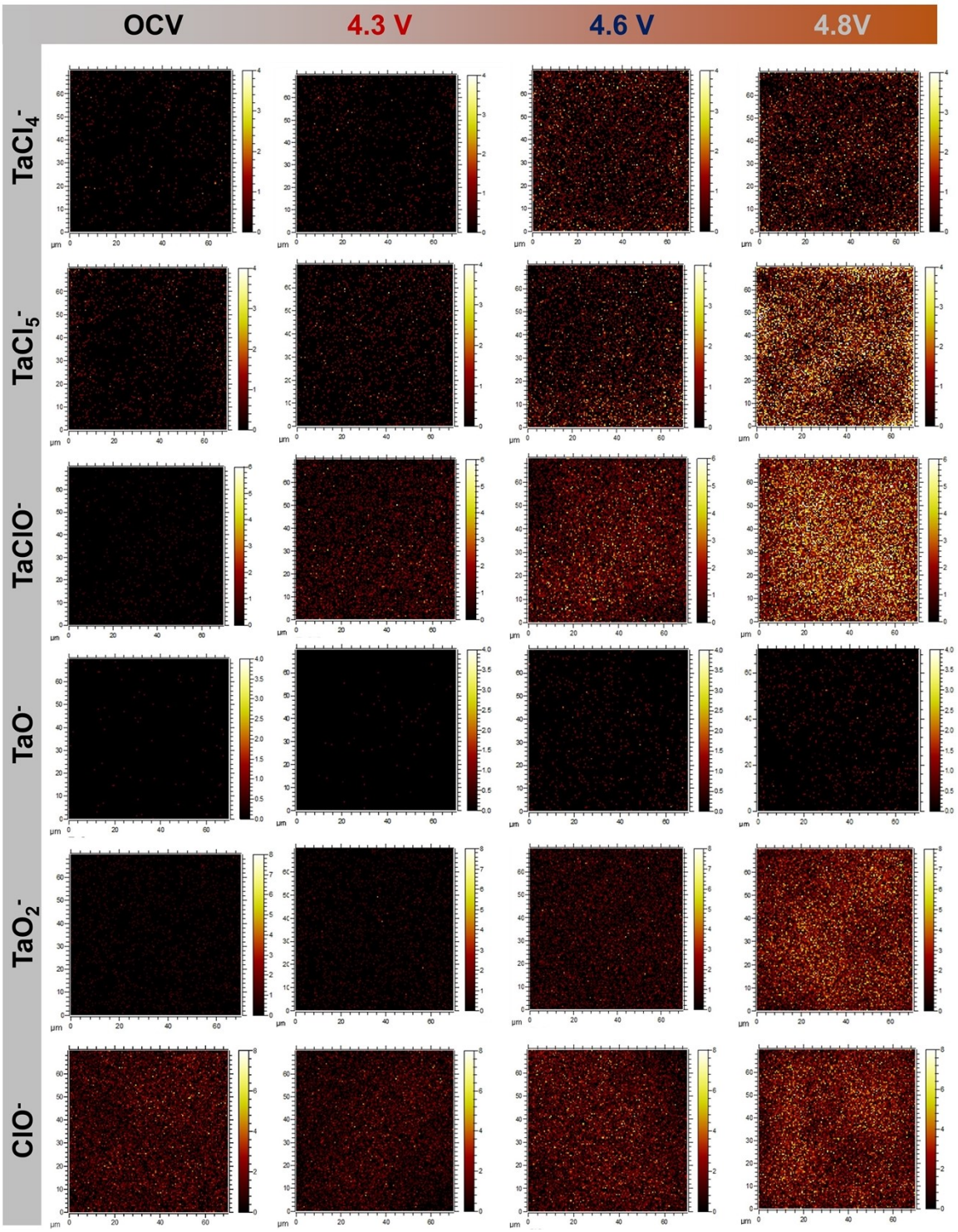

Fig. S11 ToF-SIMS exemplary secondary ion images of negatively charged fragments of the composite cathodes with the OCV and aged state at 4.3, 4.6, and 4.8 V.

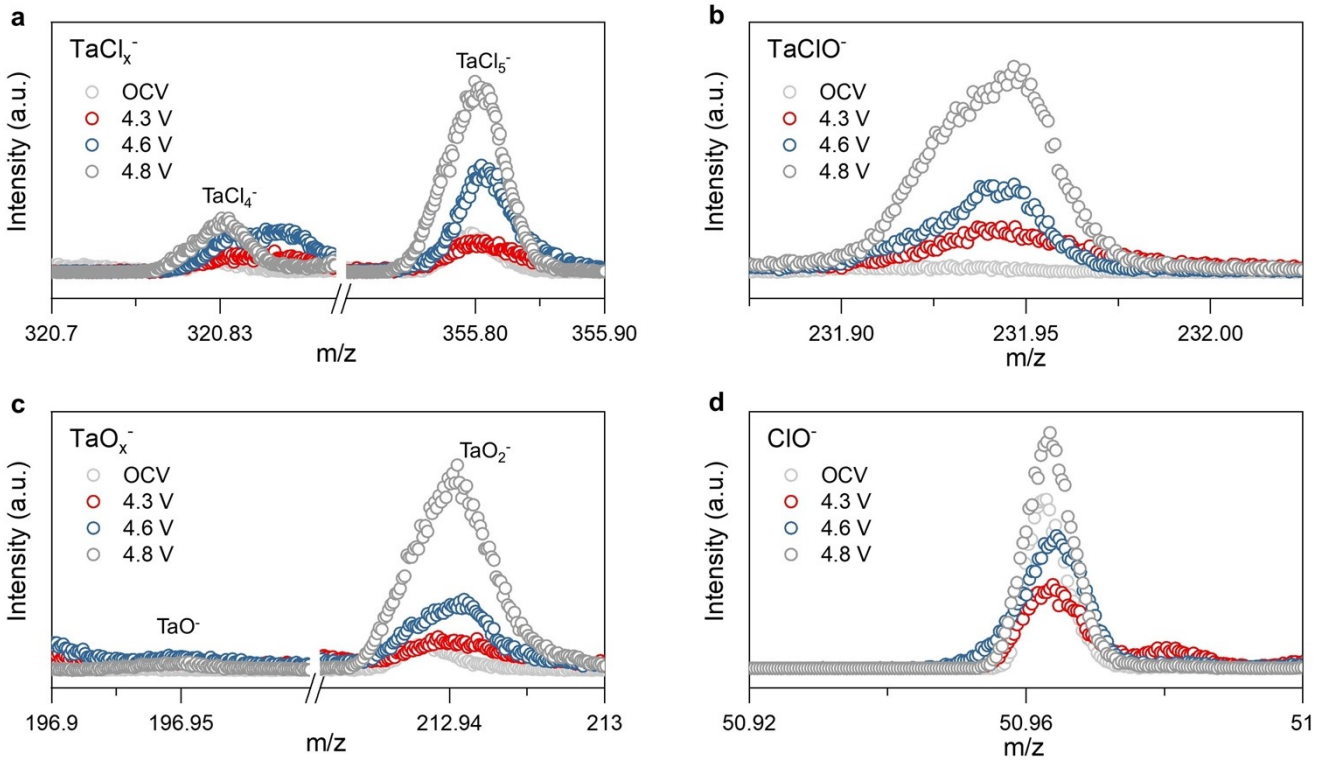

Fig. S12 ToF-SIMS mass spectra of negatively charged fragments. a-d, Evolution of the mass spectra of $TaCl_x^-$ (a), $TaClO^-$ (b), TaO_x^- (c), and ClO^- (d) fragments of the composite cathodes with the OCV and aged states at 4.3, 4.6, and 4.8 V, respectively.

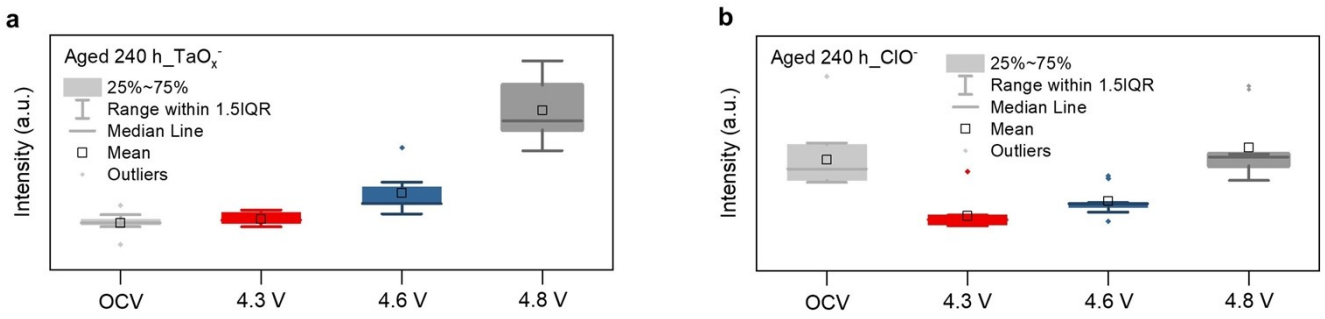

Fig. S13 a-b, Boxplots of the normalized intensity of TaO_x^- (a) and ClO^- (b) fragments of the composite cathodes with the OCV and aged states at 4.3, 4.6, and 4.8 V, respectively.

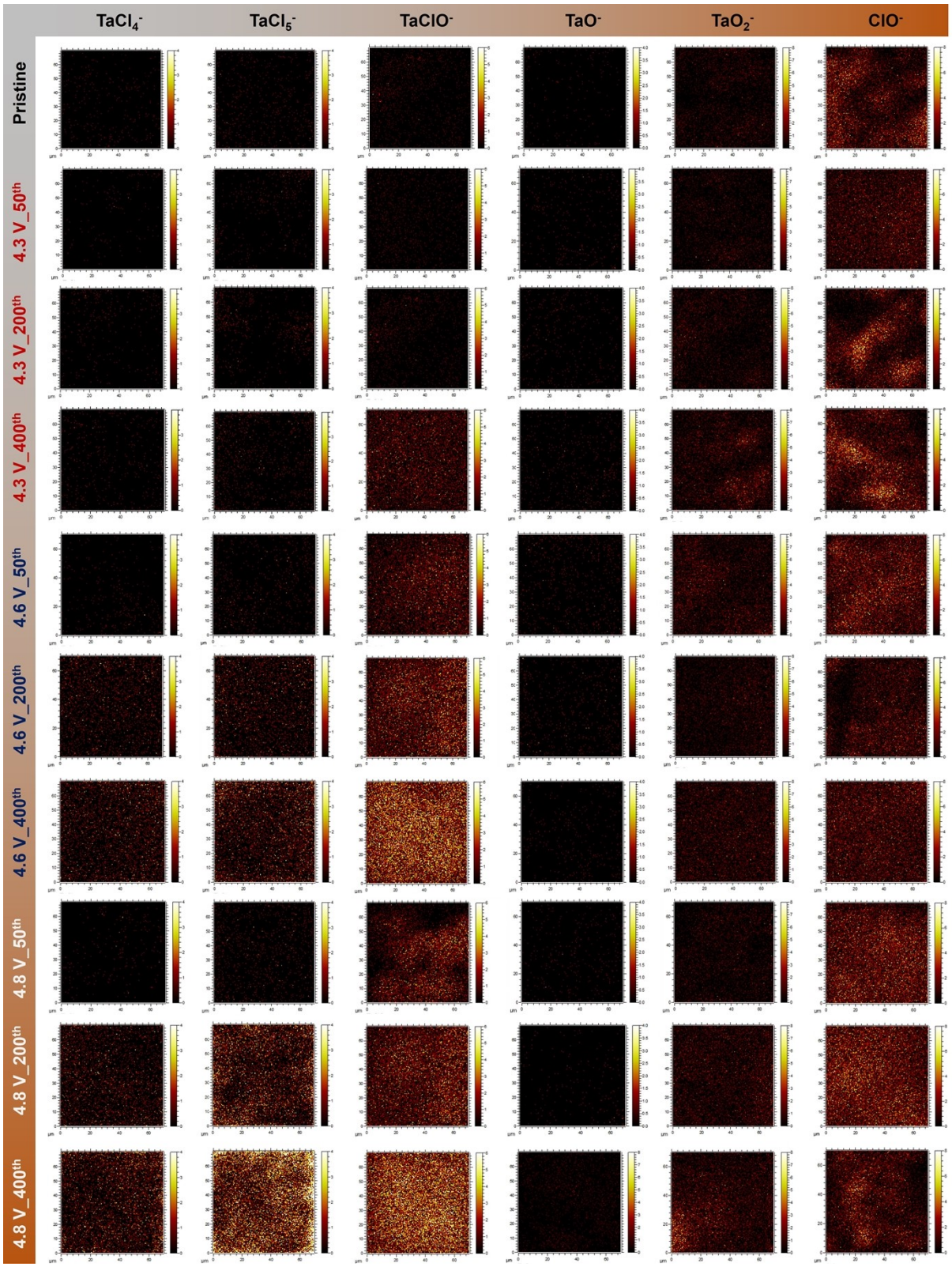

Fig. S14 ToF-SIMS exemplary secondary ion images of negatively charged fragments of the composite cathodes with the pristine and cycled state at 4.3, 4.6, and 4.8 V.

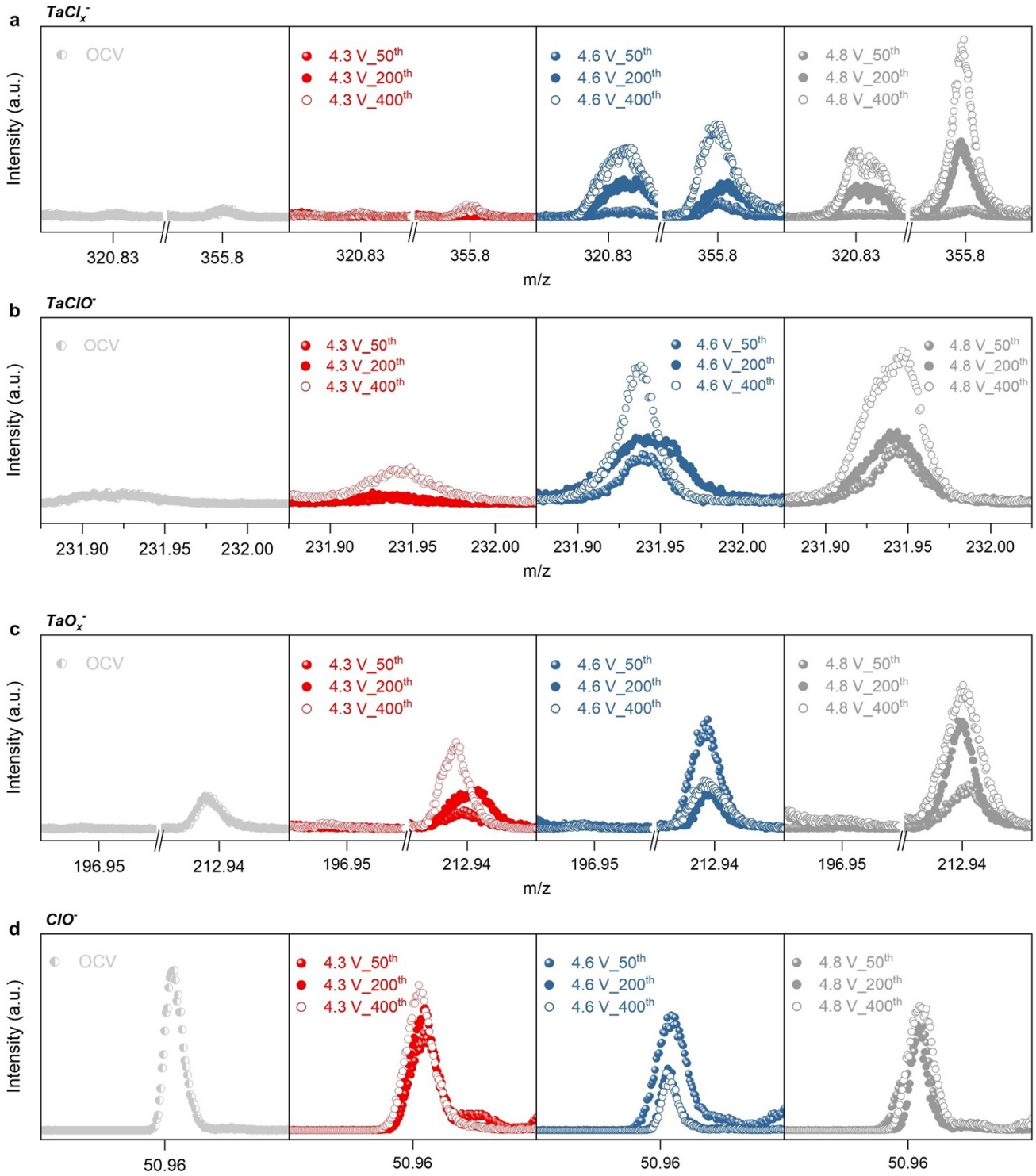

Fig. S15 ToF-SIMS mass spectra of negatively charged fragments. a-d, Evolution of the mass spectra of $TaCl_x^-$ (a), $TaClO^-$ (b), TaO_x^- (c), and ClO^- (d) fragments of the composite cathodes with the pristine and cycled states at 4.3, 4.6, and 4.8 V, respectively.

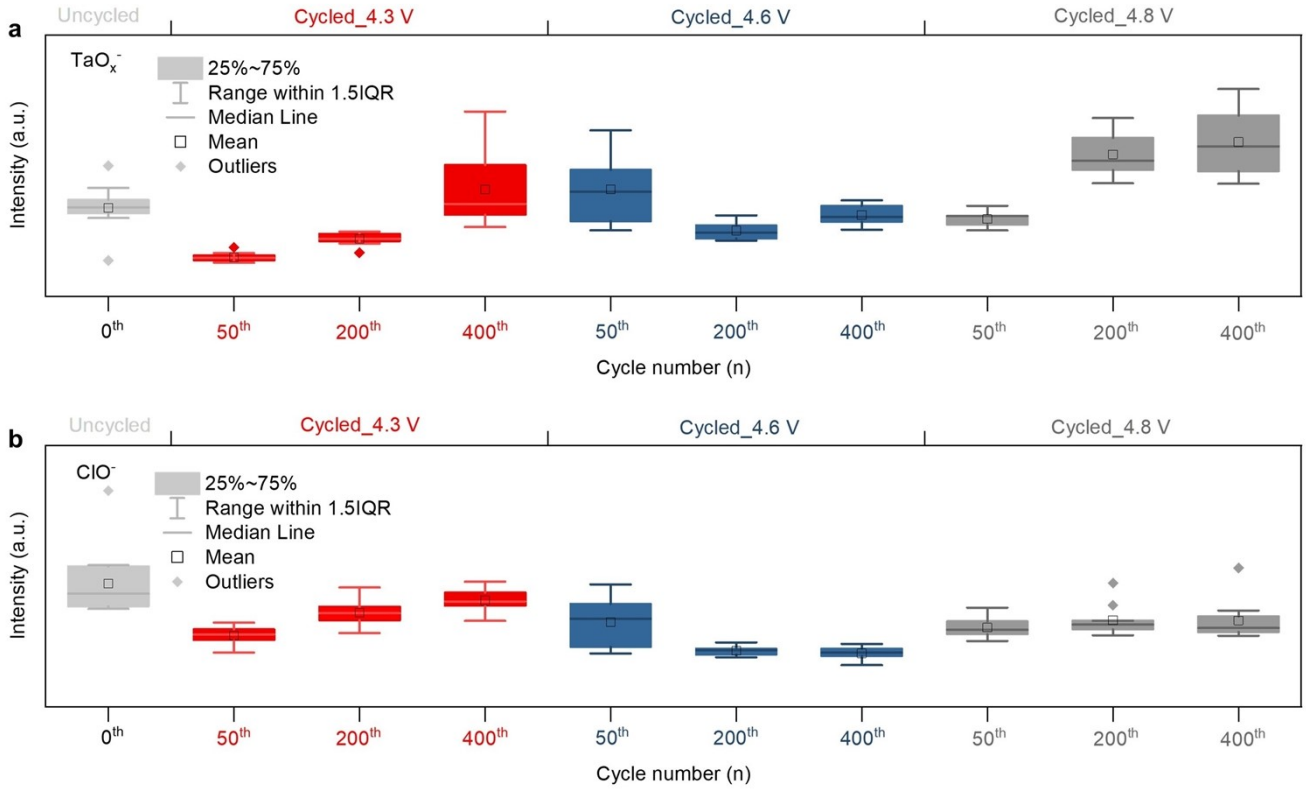

Fig. S16 a-b, Boxplots of the normalized intensity of TaO_x^- (a) and ClO^- (b) fragments of the composite cathodes with the OCV and cycled states at 4.3, 4.6, and 4.8 V, respectively.

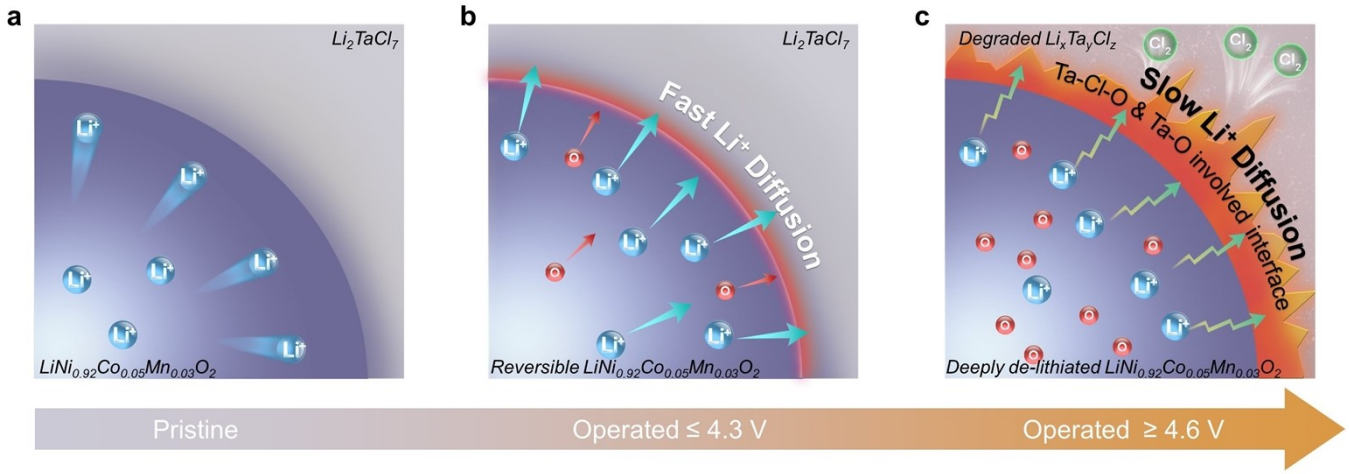

Fig. S17 Scheme diagram of the degradation pathways of Li_2TaCl_7-$LiNi_{0.92}Co_{0.05}Mn_{0.03}O_2$.

Note S1. When operated at low cut-off voltages, stable cycling can be achieved due to the good oxidation stability of Li_2TaCl_7 and reversible lithiation and de-lithiation processes of S-NCM92, particularly at cut-off voltages of 4.3 V and notably at 4.1 V. However, when operated at higher cut-off voltages of 4.6 and 4.8 V, oxidation reactions in Li_2TaCl_7 occur, leading to the decomposition of the amorphous matrix. This decomposition disrupts the Li-ions conduction network, significantly increasing the resistance of migration of Li-ions and polarization of ASSLBs. Meanwhile, the lattice oxygen liberated from the charged S-NCM92 predominantly interacts with the $TaCl_6^-$ sublattice within Li_2TaCl_7, leading to the formation of Ta-Cl-O and Ta-O species. These reactions generate side-products that obstruct Li-ion migration, significantly increasing interface resistance and adversely affecting the ASSLBs' capacity and lifespan.

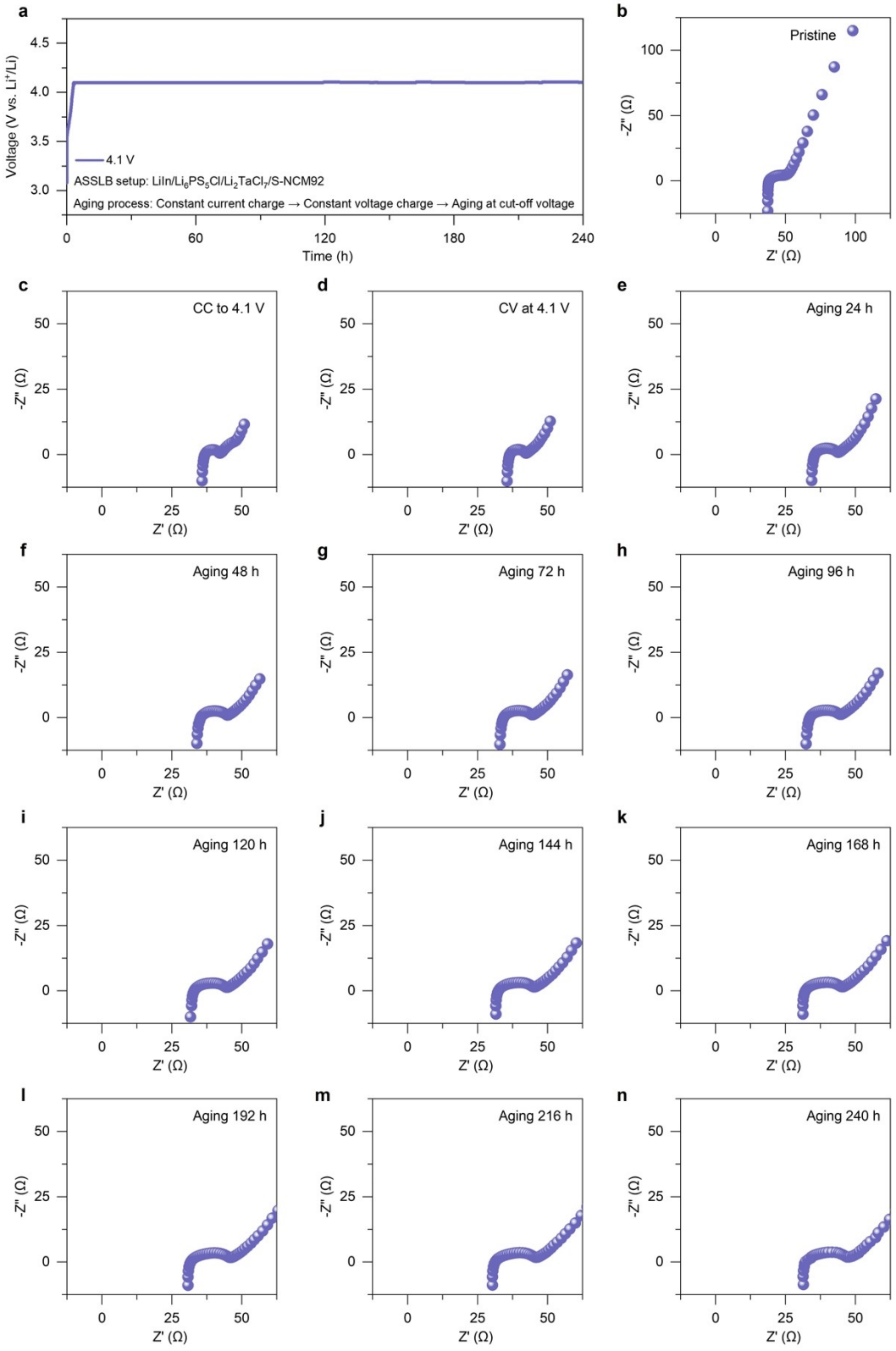

Fig. S18 a, Electrochemical curves of ASSLBs first charged to 4.1 V and then aged and held for 240 h. **b-n**, Nyquist plots of the EIS results of ASSLBs during the aging process with a constant voltage of 4.1 V.

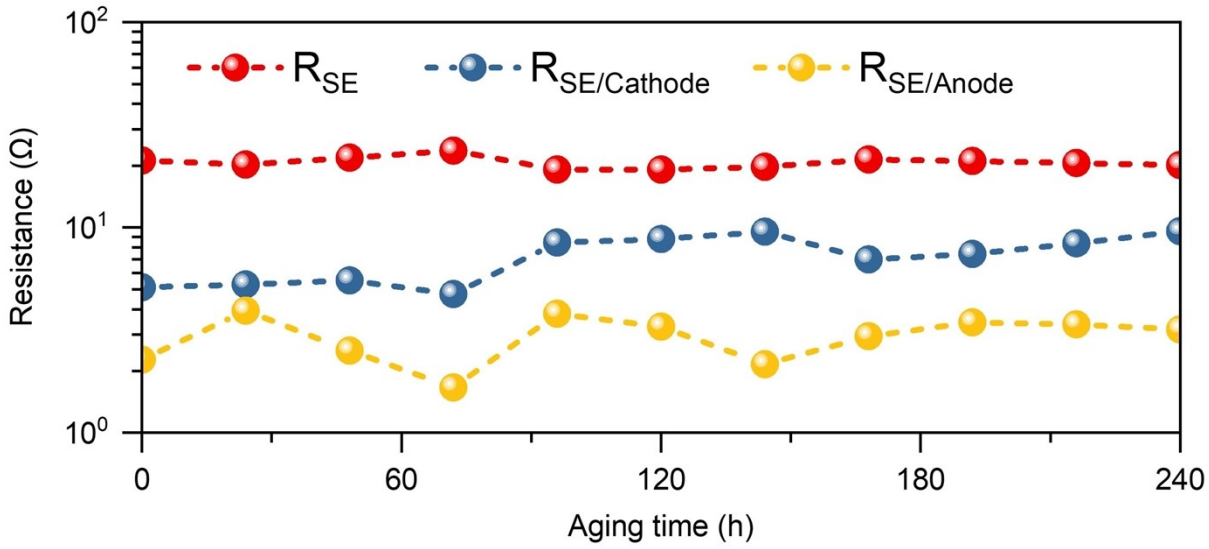

Fig. S19 Interface stability of ASSLBs as a function of aging time with a charging voltage of 4.1 V revealed by in-situ EIS. Evolution of fitted electrolyte resistance, cathode-electrolyte interface resistance, and anode-electrolyte interface resistance plotted as a function of aging time.

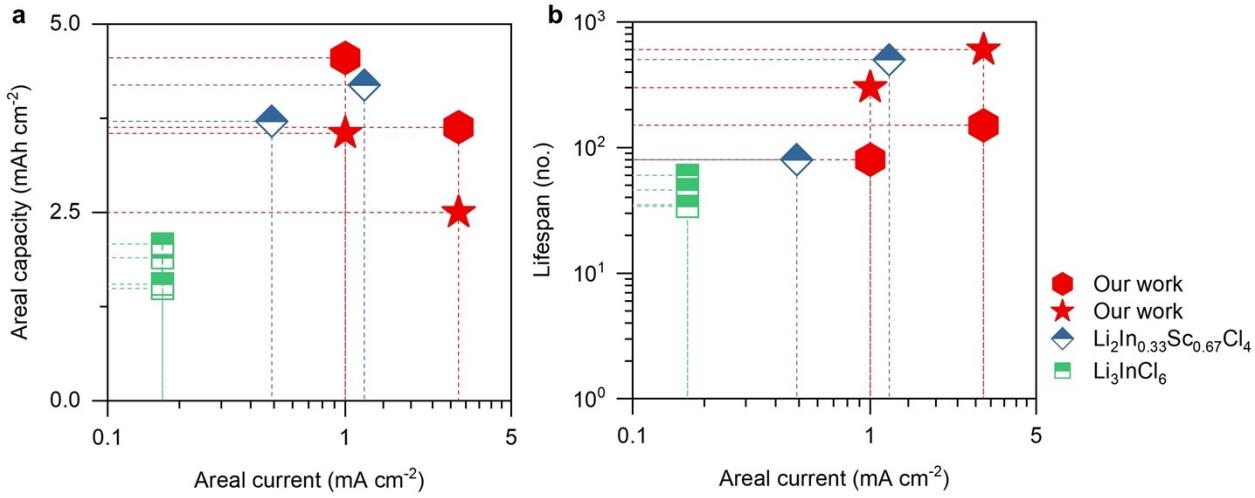

Fig. S20 a-b, Comparison of electrochemical performance of top-notch chloride SE-based ASSLBs, including areal capacity (a) and lifespan (b).

Supplementary Tables

Table S1. Comparison of electrochemical performance, including discharge capacity and lifespan, of chlorides-based ASSLB with designed areal capacity over 3 mAh cm^{-2} operated with different cut-off voltages, as exhibited in **Figure S20**.

Chlorides	Cathodes	Cut-off voltage (V)	Loading ($g\ cm^{-2}$)	Current ($mA\ cm^{-2}$)	Capacity ($mAh\ g^{-1}$)	Cycles (no.)	Retention (%)	References
$Li_2In_{0.33}Sc_{0.67}Cl_4$	LCO	4.5	52.46	1.2	80	500	100 (50 °C)	Nat. Energy 2022, 7(1): 83-93
	NCM85	4.3	21.59	0.49	172	80	108	
Li_3InCl_6	NCM622	4.2	11.9	0.17	125	70	60	ACS Energy Lett. 2022, 7, 2979−2987
		4.3			130		35	
		4.4			160		46	
		4.5			175		34	
Li_2TaCl_7	NCM92	***4.3***	***24.3***	***1***	***187.1***	***110***	***70***	***Our work***
			25.2	***3***	***144.1***	***220***	***72***	
		4.1	***23.6***	***1***	***150.2***	***200/300***	***91/80***	
			22.2	***3***	***112.1***	***600***	***82***	